UC Davis
UC Davis Previously Published Works

Title
Structure–Property Relationships of Amphiphilic Nanoparticles That Penetrate or Fuse Lipid Membranes

Permalink
https://escholarship.org/uc/item/5s27s400

Journal
Bioconjugate Chemistry, 29(4)

ISSN
1043-1802

Authors
Atukorale, Prabhani U
Guven, Zekiye P
Bekdemir, Ahmet
et al.

Publication Date
2018-04-18

DOI
10.1021/acs.bioconjchem.7b00777

Peer reviewed

Structure-property relationships of amphiphilic nanoparticles that penetrate or fuse lipid membranes

Prabhani U. Atukorale[1], **Zekiye P. Guven**[2,**], **Ahmet Bekdemir**[2,**], **Randy P. Carney**[2,**], **Reid C. Van Lehn**[3], **Dong Soo Yun**[4], **Paulo H. J. Silva**[2], **Davide Demurtas**[5], **Yu-Sang Yang**[3], **Alfredo Alexander-Katz**[3], **Francesco Stellacci**[2], and **Darrell J. Irvine**[1,2,3,4,5,6,7,8,*]

[1]Department of Biological Engineering, Massachusetts Institute of Technology, Cambridge, Massachusetts 01239, United States [2]Institute of Materials, Ecole Polytechnique Federale de Lausanne, 1015 Lausanne, Switzerland [3]Department of Materials Science and Engineering, Massachusetts Institute of Technology, Cambridge, Massachusetts 01239, United States [4]Koch Institute for Integrative Cancer Research, Massachusetts Institute of Technology, Cambridge, Massachusetts 01239, United States [5]Interdisciplinary Center for Electron Microscopy, Ecole Polytechnique Fédérale de Lausanne, 1015 Lausanne, Switzerland [6]Institute for Soldier Nanotechnologies, Massachusetts Institute of Technology, Cambridge, Massachusetts 01239, United States [7]Ragon Institute of MGH, MIT, and Harvard, Cambridge, Massachusetts 02139, United States [8]Howard Hughes Medical Institute, Chevy Chase, Maryland 20815, United States

Abstract

The development of synthetic nanomaterials that could embed within, penetrate, or induce fusion between membranes without permanent disruption would have great significance for biomedical applications. Here we describe structure-function relationships of highly water-soluble gold nanoparticles comprised of a ~1.5–5 nm diameter metal core coated by an amphiphilic organic ligand shell, which exhibit membrane embedding and fusion activity mediated by the surface ligands. Using an environment-sensitive dye anchored within the ligand shell as a sensor of membrane embedding, we demonstrate that particles with core sizes of ~2–3 nm are capable of embedding within and penetrating fluid bilayers. At the nanoscale, these particles also promote spontaneous fusion of liposomes or spontaneously embed within intact liposomal vesicles. These studies provide nanoparticle design and selection principles that could be used in drug delivery applications, as membrane stains, or for the creation of novel organic/inorganic nanomaterial self-assemblies.

Keywords

amphiphilic gold nanoparticles; water-soluble nanoparticles; membrane embedding; membrane penetration; membrane fusion

Synthetic nanomaterials that could controllably penetrate lipid membranes or promote fusion between bilayers are of significant interest as intracellular drug delivery and imaging agents. Toward this goal, many nanoparticles have been designed to exploit electrostatic interactions between cationic particles and anionic biological membranes.[1–4] However, such materials often induce membrane disruption that results in cytotoxicity. Alternative approaches involve functionalizing particles with cell-penetrating peptides, antimicrobial peptides, or other biological motifs to mediate nanoparticle entry into cells by membrane insertion with subsequent stimulation of endocytosis.[5–9] While toxicity is minimized, endosomal escape is often inefficient. Inert metallic nanoparticles ~2–5 nm in diameter capped with hydrophobic alkyl ligands have been shown to embed within synthetic lipid bilayers.[10–12] However, since these particles are intrinsically water-insoluble, organic solvents are necessary to facilitate bilayer insertion. The rational design of nanomaterials that controllably interact with lipid bilayers or cell membranes thus remains an open challenge.

We have previously studied the passive membrane transit properties of small ~2–6 nm diameter gold nanoparticles coated by an organic ligand shell of alkyl-sulfonate ligands in live mammalian cells (both tissue-derived cells and red blood cells) extensively (Fig. 1a).[13–16] These highly water soluble amphiphilic nanoparticles (amph-NPs) coated with mercapto-undecanesulfonate (MUS) or both MUS and octanethiol (OT) were found to accumulate in the cytoplasm of cells even when active endocytosis was inhibited.[13,14] Coarse-grained computational simulations suggested mechanistically that these amph-NPs embedded spontaneously within lipid membranes by reorganizing their surface ligands, 'snorkeling' the hydrophilic sulfonate endgroups to the aqueous interface while the hydrophobic alkyl chains resided within the bilayer interior.[17,18] We then extended these results to red blood cells which are naturally non-endocytic and showed that ~2–4 nm core amph-NPs interacted with and embedded within the plasma membrane of these cells.[15] Very recently, we showed by mass cytometry measurements that ~2.5–4 nm core amph-NPs were also taken up by multiple types of immune cells (dendritic cells, T cells, B cells, neutrophils, and macrophages) *in vivo*.[16] In this study, mice vaccinated with amph-NPs conjugated to a peptide antigen construct developed a potent protective immune response compared to animals treated with soluble peptide, and 100% of amph-NP-immunized mice remained tumor-free after challenge with antigen-expressing tumor cells.[16] Taken together, these *in vitro* and *in vivo* studies suggest that these amph-NPs are promising agents for drug delivery, and these findings motivated us to develop a set of design principles in terms of nanoparticle core size, surface hydrophobicity, and membrane properties that govern optimal amph-NP/ membrane interactions.

Here, we sought to address these fundamental questions by using a reductionist model membrane approach that is readily controllable. We show that dyes tethered *via* alkyl chains

to the gold core of amph-NPs can serve as environmental sensors of membrane insertion, and use this optical reporter to define how membrane properties and amph-NP composition modulate their interactions. We further characterized NP/membrane interactions by cryoEM, and show that amph-NPs can both embed within synthetic liposome bilayers or induce hemi-fusion between vesicles, depending on particle size and ligand shell composition.

Results and Discussion

Alkyl-BODIPY ligands as optical sensors of amph-NP/membrane embedding

Our recent simulations of mercapto-undecanesulfonate (MUS) and MUS/octanethiol (OT) ligand-coated amph-NPs (Fig. 1a) suggested that the organic ligand shell collapses in water to minimize solvent contact with the hydrophobic chains, but reorganizes on entry into a lipid bilayer.[17,18] Based on these simulation data and the strong distance-dependent fluorescence quenching behavior of gold,[19] we predicted that NP-tethered hydrophobic dyes might act as sensors of membrane embedding, with the dye collapsed against the particle core and quenched in aqueous solution but extended from the gold surface and fluorescing within a bilayer environment. To test this idea, we first carried out molecular dynamics simulations of the model fluorophore BODIPY tethered within the organic layer of MUS/OT NPs with a 2 nm core, to predict conformational states of a ligand-tethered dye (Fig. 1b–d, Supplementary Fig. 1a–c). We calculated the potential of mean force (PMF, the free energy change associated with changing the distance between the dye and the gold core) for MUS/OT particles in water compared to the same particles inserted in a lipid bilayer.[20,21] The minimum in the PMF-distance curve indicates the preferred equilibrium separation between the gold surface and BODIPY. These calculations predicted the dye would lie very near the gold surface in aqueous solution, but extend ~1.25 nm into the surroundings when the particles are membrane-embedded (Fig. 1c). Snapshots from these simulations showed the BODIPY ligand collapsed against the gold surface for particles in solution (Fig. 1d, top), but extending into the hydrophobic bilayer interior for embedded particles (Fig. 1d, bottom, Supplementary Fig. 1d). We expected these differences in dye localization to strongly influence fluorescence emission, as gold surfaces exhibit strong fluorescence quenching, in a manner that decays exponentially as the dye-Au separation increases.[19] In addition, BODIPY is intrinsically sensitive to the polarity of its surroundings, and is known to exhibit enhanced fluorescence in nonpolar solvents.[22,23]

To experimentally corroborate these predictions, we added BODIPY-labeled MUS/OT or MUS NPs to phosphatidylcholine (DOPC) liposomes and measured fluorescence for a range of lipid concentrations. (Precise particle batches are cited in the captions, named using the format [ligand composition]-[core diameter]; characterization data in Supplementary Information.) In the presence of liposomes, emission from labeled NPs increased significantly over the low fluorescence levels in water alone. For a fixed concentration of BODIPY-NPs, a linear increase in signal was observed with increasing liposome concentration (Fig. 1e, Supplementary Fig. 2). We confirmed by cryogenic electron microscopy (cryoEM) tomography that the appearance of BODIPY signal in MUS/OT-liposome samples correlated with spontaneous interaction and embedding of particles in DOPC membranes (Fig. 1f–g, Supplementary Video 1). In parallel, we examined BODIPY-

NP fluorescence by confocal microscopy. We previously observed that when giant multilamellar vesicles (GMVs) were co-incubated with the membrane-impermeable tracer calcein and MUS/OT NPs, calcein remained external while particles absorbed throughout the GMVs.[17] Extending these observations here, we found that 2.4 nm-core MUS NPs also penetrated GMV membranes (Fig. 1h–j), while excess NPs in the surrounding solution did not fluoresce above background (Fig. 1i) despite the clear presence of free particles (visible by the dark brown color of the solution). The lack of BODIPY-MUS fluorescence in solution was not due to quenching by calcein and lipid autofluorescence did not contribute to NP-GMV signal (Supplementary Fig. 3a–c). Thus, the particle-bound BODIPY ligand serves as an optical sensor for membrane-embedded nanoparticles.

Membrane electrostatics and fluidity govern microscale amph-NP/membrane interactions

We used this BODIPY-ligand sensor to assess the role of the organic shell and lipid compositions on amph-NP/membrane interactions. BODIPY-labeled particles were prepared with three distinct ligand compositions but comparable gold core diameters (~2–2.5 nm, Supplementary Table 1): MUS, MUS/OT 2:1, and MUS/brOT 2:1 (incorporating branched octanethiol, Fig. 1a, to test the impact of ligand organization/packing on membrane interactions).[13] Flow cytometry measurements made on thousands of GMVs showed statistically equivalent absorption of all three particle compositions into DOPC membranes (Fig. 2a–b). Qualitatively identical behavior was observed for MUS/OT 1:1 NPs with ~2–2.5 nm core sizes (data not shown).

We next evaluated how membrane charge and liquid ordering influence interactions with amph-NPs. Because mammalian cell membranes have a net negative charge,[1] we compared the interaction of MUS/OT NPs with zwitterionic DOPC GMVs or anionic GMVs composed of 80/20 mol/mol DOPC/DOPG (Supplementary Fig. 4a) in water or phosphate-buffered saline (PBS). As shown in Fig. 2c(i-ii), MUS/OT particles strongly absorbed through DOPC GMV membranes in water within 1 hr at 25°C, but were excluded from DOPC/DOPG membranes. Quantification of confocal signals showed a 4.9-fold lower BODIPY signal in DOPC/DOPG vs. DOPC membranes (Fig. 2d). However, in the presence of physiologic electrolytes (PBS), the anionic particles also avidly embedded and penetrated DOPC/DOPG GMVs (Figs. 2c(iii) and 2d).

To assess the impact of membrane phase/fluidity on NP absorption, we compared GMVs of three different compositions: DOPC (T_m=−20°C), DPPC (T_m=41°C), and 50/50 mol/mol DOPC/DPPC (Supplementary Fig. 4b). Confocal imaging and flow cytometry analysis of MUS/OT NPs incubated with these GMVs for 1 hr at 25°C revealed that while BODIPY-labeled NPs interacted highly with fluid DOPC and DOPC/DPPC GMVs, these particles were completely excluded from gel-phase DPPC GMVs (Fig. 2c(iv-v), Fig. 2e). Since cholesterol is known to impact membrane stiffness,[24,25] we compared BODIPY-MUS/OT interactions with DOPC GMVs with or without 25% cholesterol and found that cholesterol had no impact on NP absorption (Supplementary Fig. 4c). To distinguish effects of membrane phase from a structural incompatibility of nanoparticles embedding in thicker DPPC bilayers,[26] we incubated DPPC GMVs with BODIPY-MUS/OT NPs at 25°C, 37°C, or 50°C in water and analyzed uptake using both confocal microscopy and flow cytometry.

There was essentially no NP interaction with gel-phase GMVs even after 2 hr at 25°C (Fig. 2f(i)). However, after only 5 min at 37°C, particles began to absorb to the outer periphery of DPPC vesicles and by 1 hr had penetrated throughout the vesicles (Fig. 2f(ii-iv)). NP uptake kinetics assessed quantitatively by flow cytometry showed that within 10 min, NP absorption into GMVs at 37°C increased 5-fold compared to 25°C (Fig. 2g). These data suggest that membrane fluidity significantly influences both the kinetics and equilibrium quantity of embedding NPs.

Core size and surface composition govern nanoscale amph-NP/membrane interactions

To gain insight into nanoscale NP/membrane interactions, we next examined particle size and surface composition influences on interactions with liposomes using cryoEM. First, we compared MUS particles with mean core sizes ranging from 1.7 to 4.2 nm (Fig. 3a, d, g, and Supplementary Table 1). We incubated these particles at 0.28 mg/mL or 0.56 mg/mL with DOPC liposomes in water at 25°C, vitrified these samples in liquid nitrogen, and then imaged *via* cryoEM. At the lower concentration, the majority of MUS-1.7 particles were found to be associated with liposomes without significant clustering or disturbance of liposome morphology (Fig. 3b, Supplementary Fig. 5a). Doubling the NP concentration led to a clustering of particles and liposomes but did not appear to alter vesicle morphology significantly (Fig. 3c and Supplementary Fig. 5b). By contrast, MUS-2.4 particles at 0.28 mg/mL induced hemi-fusion of adjacent bilayers, with striking faceting of liposome-liposome junctions and two-dimensional particle alignment along fusion planes (Fig. 3e, Supplementary Fig. 5c); increasing NP concentration led to increased vesicle aggregation (Fig. 3f and Supplementary Fig. 5d). Increasing the core diameter further, MUS-4.2 particles (similar to MUS-1.7) interacted with liposomes but did not induce changes in liposome morphology at either concentration (Fig. 3h, i, Supplementary Fig. 5e, and Supplementary Fig. 5f for an alternate batch of larger MUS-5.0 particles). Notably, MUS-2.4 particles have a core diameter in the range predicted as most favorable for stable insertion in bilayers by our earlier simulations.[17] To further establish the range of core diameters eliciting fusion of vesicles, a separate batch of particles with a core diameter of 3.2±0.9 nm was imaged with liposomes, and also induced similar vesicle hemi-fusion (MUS-3.2, Supplementary Table 1 and Supplementary Fig. 6a–b).

We next evaluated the impact of ligand shell hydrophobicity on NP/membrane interactions within this specific core size range. We prepared MUS/OT 1:1–2.6 particles incorporating 50% of hydrophobic OT (Fig. 3j, Supplementary Table 1). When incubated with DOPC liposomes, MUS/OT 1:1–2.6 NPs induced hemi-fusion and aggregation between liposomes analogous to the similarly-sized MUS-2.4 NPs, but without faceting of conjoined membranes (Fig. 3k, Supplementary Fig. 7).

To validate that this observed fusion behavior was not a cryoEM sample preparation artifact, we made fluorescence resonance energy transfer (FRET)-based measurements of lipid mixing using two populations of dye-labeled DOPC liposomes mixed with particles at 25°C. A 1:1 mixture of liposomes labeled with either a FRET donor (0.1 mol% DiD, ex/em 644/663 nm) or a FRET acceptor (0.1 mol% DiR, ex/em 748/780 nm) was prepared. MUS or MUS/OT particles (absorbance spectra shown in Supplementary Fig. 8) were added to the

liposomes, samples were excited at 644 nm, and fluorescence emission spectra across the donor/emitter wavelengths were measured. As a positive control, liposomes containing both dyes were prepared as a measure of maximal lipid mixing/FRET; gold particles with a 4.8 nm core coated with 5 KDa PEG (Supplementary Table 1), which we expected to weakly interact with liposomes, were included as a negative control. As shown in Fig. 4a, by 20 min, both MUS-2.4 and MUS/OT 1:1–2.6 particles that exhibited evidence for hemi-fusion/fusion *via* cryoEM showed strong FRET signals. Quantification of the acceptor-donor emission ratios showed that these particle compositions induced ~82% of maximum lipid mixing at 20 min, compared to PEGylated particles that had FRET ratios less than 2% of the positive control; maximum fusion was achieved after 2.5 hr (Fig. 4b). Thus, bulk analysis of particle-liposome interactions was concordant with cryoEM evidence of vesicle fusion induced by both MUS and MUS/OT 1:1 particles with core diameters in the 2–3 nm range.

Nanomaterials that can spontaneously embed within membranes and promote membrane fusion with minimal cytotoxicity have significant applications in drug delivery and imaging. Cell membrane embedding enables drug cargo-carrying nanoparticles to bypass endocytosis and gain direct entry into the cell cytosol, thereby minimizing any cargo degradation that occurs during endosome shuttling through the endo-lysosomal pathway. Cationic nanoparticles[1–4], cell-penetrating peptides[5–7], and antimicrobial peptides[5–7] have been developed for their spontaneous membrane interaction properties, but severe cytotoxicity and entrapment in endosomes often limits their utility. The discovery of new nanomaterials that could interact with biological membranes without causing bilayer disruption thus remains of great interest.

The amphiphilic gold nanoparticles described here exhibit many characteristics that could be ideally suited to the challenge of intracellular delivery, and here we sought to investigate the structure-property relationships of spontaneous NP/membrane interactions of amphiphilic MUS and MUS/OT NPs on both a micro- and nanoscale. For microscale interaction experiments, we used hydrophobic BODIPY-alkyl grafts on MUS and MUS/OT NPs that could extend from the gold core when bilayer-inserted, fluoresce, and serve as membrane embedding sensors. These *in situ* sensors revealed that interactions of these anionic NPs with anionic fluid membranes was minimal in water, but occurred rapidly in the presence of electrostatic shielding by physiologic levels of electrolytes. By contrast, NPs were excluded from gel-phase membranes. Given that both electrostatics and fluidity are central governing properties of biological membranes, these findings suggested that amph-NPs are highly suitable for physiological applications.

For nanoscale interaction experiments, we used cryoEM imaging and FRET-based measurements to show that amph-NPs with a metal core diameter of ~2–3.5 nm were capable of promoting significant hemi-fusion between fluid lipid membranes, mediated by particle alignment along membrane-membrane interfaces. Notably, our earlier computational studies predicted that this core diameter range was most favorable for bilayer interaction.[17] Metallic nanoparticles with organic ligand shells have also been used for membrane embedding but, since this interaction is non-spontaneous and relies on the use of harsh organic solvents to drive the interaction, their application in biology, physiology, and medicine is also limited.[10–12]

Conclusions

In prior studies, we found that small (<5 nm) sulfonate-functionalized amphiphilic gold nanoparticles are capable of penetrating the membranes of live cells under physiological conditions, in the presence of serum, without substantial cellular cytotoxicity. Here we employed a reductionist system to understand at the micro- and nano-scale level how nanoparticle-membrane interactions occur. We found that membrane penetration by amph-NPs is promoted by physiological salt conditions and requires a fluid bilayer. Further, at the nanoscale, we find a clear size-dependent control of NP-membrane interactions, where particles with a core size of ~2.5 nm showing an ability to promote hemifusion between adjacent bilayers, while larger and smaller particles exhibit only surface binding to membranes. These nanoscale membrane fusion events are likely not restricted to the precise ligand shell chemistry studied here, as energy-independent uptake of small nanoparticles with other types of surface functionalities (anionic and zwitterionic) have also been reported.[27] Such interactions may make these intermediate-diameter particles of interest for applications in cellular labeling and drug delivery.

Undoubtedly, cellular interaction events *in vivo* or even in cell culture are more complex than the purified nanoparticle/buffer/lipid membrane systems analyzed here; this would especially true if strongly-bound protein coronas develop around amph-NPs *in vivo*. The reductionist approach taken here importantly allowed clear observation of nanoscale interactions between particles and membranes that would have been problematic when working (for example) with serum-containing media. However, consistent with our prior cell-penetrating observations of these nanomaterials in live cell experiments, work by ourselves and others suggests that very small particles as studied here will not necessarily be dramatically altered in terms of protein corona or aggregation under physiological conditions. For example, Boselli et al. reported that ultrasmall gold nanoparticles can show very weak and readily dislodged protein binding in serum, depending on the surface chemistry of the particles.[28] Very small particles are also more resistant to aggregation in biological media, due to presence of a dominant energy minimum between particles prior to close contact.[29] In our own prior studies, we found that amph-NPs were resistant to protein adsorption and have high stability against aggregation in physiologic conditions.[30] Whether the membrane fusion phenomena observed here will also translate to living cell systems is a subject of ongoing study.

In summary, these findings define size and composition criteria leading to amphiphilic nanoparticles that can only bind to, adsorb within, or promote fusion between lipid bilayers. Within these defined compositional ranges, these particles may find applications in drug delivery, as membrane stains, or for the creation of unique nanomaterial-lipid self-assemblies. The novel environmental sensor dye strategy described here should also be of general use in the nanomaterials community for studying local changes in the microenvironment of nanoparticles.

Methods

Materials

HAuCl$_4$ salt, OT ligand, and calcein were purchased from Sigma. BODIPY 630/650-X succinimidyl ester was purchased from Invitrogen. MUS ligands were prepared in-house as described previously.[13] All lipids and cholesterol were purchased from Avanti Polar Lipids and used as received. Control PEGylated gold particles were purchased from Sigma-Aldrich.

Gold nanoparticle synthesis, characterization, & labeling

We used a modified one-phase Brust-Schiffrin synthesis to prepare MUS and MUS/OT NPs.[31] Briefly, a solution of 0.9 mmol HAuCl$_4$ prepared in ~200 mL ethanol was mixed with an equimolar mixture of thiol ligands prepared in methanol and allowed to stir for 15 min. A saturated solution of NaBH$_4$ in ethanol was then added drop-wise and the reaction was stirred for 3 hr. The flask was placed at 4°C overnight and particle precipitates were isolated by filtration using qualitative filter paper and washed thoroughly in ethanol, methanol, and acetone. Particle powders were allowed to dry completely. Before use, ~10 mg dry NPs were dissolved in 1 mL water, centrifuged at 14,000 × g for 2 min, and insoluble NPs were removed by discarding the resulting pellet. NPs were imaged using transmission electron microscopy (TEM) and core size distributions were determined using ImageJ software. For characterization of the MUS/OT ratio on particle surfaces, 25 μL of NP solution (10 mg/mL in D$_2$O) was added to 0.5 mL of iodine solution in MeOD (10 mg/mL). Samples were sonicated for 15 min to allow etching of the gold core and release of MUS and OT ligands into the solution while the resulting gold iodide precipitated to the bottom. The supernatant was transferred into NMR tube 5 mm diameter (Wilmad ® 400 MHz). ^{1}H NMR analysis was conducted with a Bruker 400 MHz AVANCE-400 BBI$_z$:^{1}H probe instrument. All NMR experiments were collected with 16–32 scans with automatic tuning and matching settings. NMR spectra for all mixed ligand batches and a representative MUS batch are included in Supplementary Fig. 9.

The HS-C$_{11}$-BODIPY dye construct was prepared in-house by conjugation of an alkylthiol linker to BODIPY 630/650-X, succinimidyl ester. MUS and MUS/OT NPs were labeled by place-exchange of HS-C11-BODIPY with NP surface ligands by incubating 30 μmoles of dye construct per mg of NPs over 2–4 days at 25°C with constant shaking or stirring. Labeled AuNPs were purified and separated from excess dye by precipitation and thorough washing in acetone at least 5–10 times. Purified NPs were dried overnight before use.

GMV synthesis & preparation

To synthesize GMVs, lipid stocks in chloroform were added to glass scintillation vials, where total lipid was 1 μmole per vial. When fluorescent lipid tracers were necessary to label GMVs, dyes were added at 0.5 mol%. Chloroform was allowed to evaporate overnight at 25°C, leaving lipid films on glass. Uncapped vials were then incubated in a water bath at 70°C for > 6 hr. Sucrose buffer (50 mM in water or PBS) was then added at 2 mL per vial, and vials were capped and further incubated at 70°C overnight, allowing GMVs to form. After first cooling to 25°C, GMVs were gently harvested without agitation or mixing the following day. For studies involving membrane electrostatics, we used DOPC GMVs in

water, 80% DOPC/20% DOPG GMVs in water, and 80% DOPC/20% DOPG GMVs in PBS. For studies involving membrane phase, we used DOPC GMVs, 50% DOPC/50% DPPC GMVs, and DPPC GMVs all in water. For testing of effects of membrane cholesterol, we used DOPC GMVs and 75% DOPC/25% cholesterol GMVs in water. Where indicated, we used 0.5 mol% of a 18:1 NBD-PE (1,2-dioleoyl-*sn*-glycero-3-phosphoethanolamine-N-(7-nitro-2–1,3-benzoxadiazol-4-yl) lipid tracer in specific GMV formulations.

Liposome synthesis

To prepare unilamellar liposomes ~80 nm in diameter, we prepared lipid films at 1 μmole lipid per glass scintillation vial, reconstituted in 200 μL water, and vortexed for 30 sec every 10 min for 1 hr. Hydrated lipid solutions were then transferred to 1.5 mL Eppendorf tubes and sonicated with a probe sonicator for 5 min on ice with alternating cycles of 6W and 3W for 30 sec intervals. Liposomes were cooled to 25°C before use.

Computational simulations

The potential of mean force (PMF) for moving the BODIPY fluorophore away from the NP surface was calculated using atomistic molecular dynamics simulations. We modeled MUS/OT 2:1 NPs with a 2 nm gold core (38 MUS ligands, 20 OT ligands, and 1 grafted BODIPY ligand per NP). The NP was modeled using a recent parameterization of mixed-monolayer-protected NPs based on the GROMOS 54a7 force field.[32–34] BODIPY was parameterized using a 'building block' approach using a combination of existing molecules in the GROMOS library and quantum chemical calculations.[35] The PMF was calculated using the weighted histogram analysis method[20,21] from umbrella sampling simulations of a NP either in solution or embedded in the bilayer. All simulations were performed with Gromacs version 4.6.1.[36] Detailed methods are included in Supplementary Methods.

Confocal microscopy

Confocal samples were prepared in 8-well LabTek chambers (Nunc) by adding GMVs to 50 mM glucose in water/PBS containing MUS or MUS/OT NPs at a 0.28 mg/mL final concentration. GMV harvests in sucrose were mixed 1–2× with a pipette and added at a 1:4 ratio in each sample well. Samples were rocked back and forth after preparation and there was no additional mixing of GMVs with MUS or MUS/OT NPs in the wells. Samples were incubated for 1 hr at 25°C, unless otherwise noted. Samples were imaged with a LSM 510 confocal microscope (Carl Zeiss). Z-stacks were collected using an optical slice thickness of 1 μm, and images were analyzed with Zeiss LSM software.

Flow cytometry

Flow cytometry samples were prepared in 96-well round-bottom plates (BD) or polystyrene flow cytometry tubes (BD Falcon). We first prepared solutions of 50 mM glucose in water/PBS with MUS or MUS/OT NPs at a 0.28 mg/mL final concentration in sample wells. GMV harvests in sucrose were mixed 1–2× with a pipette and added at a 1:4 ratio per sample well. Samples were rocked gently back and forth after preparation with was no additional mixing in the wells. Samples were incubated for 1 hr and 25°C, unless otherwise

noted. Samples were then analyzed with a LSR Fortessa HTS flow cytometer (BD) and data was analyzed using FlowJo software.

Cryogenic transmission electron microscopy

Cryo TEM samples were prepared in 100 μL volumes. MUS or MUS/OT NPs were first prepared in 70 μL water and 30 μL of liposomes were added (to yield 150 nmole of total lipid) before gentle mixing 1–2× with a pipette. NPs were added for a final concentration of 0.28 mg/mL or 0.56 mg/mL as noted. Samples were incubated for 1 hr at 25°C before sample prepation for cryoEM, unless otherwise noted. For preparation, 3 uL of the NP/ liposome sample was dropped on a lacey copper grid coated with a continuous carbon film and blotted to remove excess sample without damaging thecarbon layer by a Gatan Cryo Plunge III. The grid was mounted on a Gatan 626 single tilt cryo-holder equipped in the TEM column. The specimen and holder tip were cooled down by liquid nitrogen, which was maintained during transfer into the microscope and subsequent imaging. To avoid sample damage under the electron beam, the minimum required dose was used for imaging on a JEOL 2100 FEG microscope. The microscope was operated at 200 kV and with a magnification in the ranges of 10,000–60,000 for assessing particle size and distribution. All images were recorded on a Gatan 2kx2k UltraScan CCD camera.

Grids for tomograms were prepared in a commercial vitrification system (Vitrobot Mark IV, FEI, Netherlands) with 100% humidity at 22°C. 4μl of sample was pipetted on the lacey carbon grid (300 mesh, Electron Microscopy Science, Hatfield, PA), which was glow discharged for 3 seconds beforehand. Prior to plunge freezing, excess sample was blotted with a blotting force of −15 for 2 seconds. After plunge freezing, the grids were transferred at −178°C into a Gatan 626 cryo-holder (Gatan inc. Warrendale, PA) and imaged in a FEI Tecnai F20 microscope (FEI) operated at 200kV. Tomograms were aligned and reconstructed from a tilt series which were acquired between ±55° with 2 degree increments. The total electron dose for a tomogram was 30 e/Å^2 and it was acquired using magnification 50000× (pixel size 0.2 nm) with the defocus value ranging between −3 to −5 μm. Images were recorded by a FalconIII camera (4096 × 4096 pixels, FEI). Alignments of the images and reconstructions of the tomograms were done using 3DInspect (FEI).

FRET experiments

DOPC liposomes containing 0.1 mol% of the lipid tracers DiD (1,1'-dioctadecyl-3,3,3',3'-tetramethylindodicarbocyanine perchlorate) or DiR (1,1'-dioctadecyl-3,3,3',3'-tetramethylindotricarbocyanine iodide) were prepared as described above. Gold nanoparticles (0.28 mg/mL) were incubated at 25°C in a 96-microwell plate with a 1:1 mixture of DiD liposomes and DiR liposomes at the same total NP-to-lipid ratio as for cryoEM samples. At specific time points, samples were excited at 644 nm and emission was measured from 658–800 nm. For positive control samples, liposomes were prepared with both DiD and DiR, each at 0.1 mol%. All fluorescence measurements were made with a Tecan Infinite Pro 200 plate reader.

Statistics

Statistical analyses are detailed throughout the figures. Prism 5.0 (GraphPad Software) was used to analyze data by one-way or two-way analysis of variance (ANOVA) with Bonferroni post-test for comparison of specific groups or unpaired, two-tailed Student's *t*-test. *P* values less than 0.05 were considered statistically significant. All values are reported as the mean ± standard error of independent biological replicates.

Supplementary Material

Refer to Web version on PubMed Central for supplementary material.

Acknowledgements

References

1. Console S, Marty C, García-Echeverría C, Schwendener R & Ballmer-Hofer K (2003) Antennapedia and HIV Transactivator of Transcription (TAT) 'Protein Transduction Domains' Promote Endocytosis of High Molecular Weight Cargo upon Binding to Cell Surface Glycosaminoglycans. J. Biol. Chem 278, 35109–35114. [PubMed: 12837762]

2. Goodman CM, McCusker CD, Yilmaz T & Rotello VM (2004) Toxicity of Gold Nanoparticles Functionalized with Cationic and Anionic Side Chains. Bioconjug. Chem. 15, 897–900.

3. Leroueil PR, Berry SA, Duthie K, Han G, Rotello VM, McNerny DQ, Baker JR, Orr BG, Banaszak Holl MM (2008) Wide Varieties of Cationic Nanoparticles Induce Defects in Supported Lipid Bilayers. Nano Lett. 8, 420–424. [PubMed: 18217783]

4. Dreaden EC, Alkilany AM, Huang X, Murphy CJ & El-Sayed MA (2012) The golden age: gold nanoparticles for biomedicine. Chem. Soc. Rev 41, 2740–2779. [PubMed: 22109657]

5. Ciobanasu C, Siebrasse JP & Kubitscheck U (2010) Cell-Penetrating HIV1 TAT Peptides Can Generate Pores in Model Membranes. Biophys. J 99, 153–162. [PubMed: 20655843]

6. Zorko M & Langel Ü (2005) Cell-penetrating peptides: mechanism and kinetics of cargo delivery. Adv. Drug Deliv. Rev 57, 529–545. [PubMed: 15722162]

7. Mishra A et al. Translocation of HIV TAT peptide and analogues induced by multiplexed membrane and cytoskeletal interactions. (2011) Proc. Natl. Acad. Sci 108, 16883–16888. [PubMed: 21969533]

8. Zhang L, Rozek A & Hancock REW (2001) Interaction of Cationic Antimicrobial Peptides with Model Membranes. J. Biol. Chem 276, 35714–35722. [PubMed: 11473117]

9. Langham AA, Ahmad AS & Kaznessis YN (2008) On the Nature of Antimicrobial Activity: A Model for Protegrin-1 Pores. J. Am. Chem. Soc 130, 4338–4346. [PubMed: 18335931]

10. Rasch MR, Yu Y, Bosoy C, Goodfellow BW & Korgel BA (2012) Chloroform-Enhanced Incorporation of Hydrophobic Gold Nanocrystals into Dioleoylphosphatidylcholine (DOPC) Vesicle Membranes. Langmuir 28, 12971–12981. [PubMed: 22897240]

11. Rasch MR, Rossinyol E, Hueso JL, Goodfellow BW, Arbiol J, & Korgel BA (2010) Hydrophobic Gold Nanoparticle Self-Assembly with Phosphatidylcholine Lipid: Membrane-Loaded and Janus Vesicles. Nano Lett. 10, 3733–3739. [PubMed: 20731366]

12. Bonnaud C, Monnier CA, Demurtas D, Jud C, Vanhecke D, Montet X, Hovius R, Lattuada M, Rothen-Rutishauser B, & Petri-Fink A (2014) Insertion of Nanoparticle Clusters into Vesicle Bilayers. ACS Nano 8, 3451–3460. [PubMed: 24611878]

13. Verma A, Uzun O, Hu Y, Hu Y, Han H-S, Watson N, Chen S, Irvine DJ, & Stellacci F (2008) Surface-structure-regulated cell-membrane penetration by monolayer-protected nanoparticles. Nat. Mater 7, 588–595. [PubMed: 18500347]

14. Jewell CM, Jung J-M, Atukorale PU, Carney RP, Stellacci F, & Irvine DJ (2011) Oligonucleotide Delivery by Cell-Penetrating 'Striped' Nanoparticles. Angew. Chem 123, 12520–12523.

15. Atukorale PU, Yang Y-S, Bekdemir A, Carney RP, Silva PJ, Watson N, Stellacci F, & Irvine DJ(2015) Influence of the glycocalyx and plasma membrane composition on amphiphilic gold nanoparticle association with erythrocytes. Nanoscale 7, 11420–11432. [PubMed: 26077112]

16. Yang Y-SS, Atukorale PU, Moynihan KD, Bekdemir A, Rakhra K, Tang L, Stellacci F, & Irvine DJ (2017) High-throughput quantitation of inorganic nanoparticle biodistribution at the single-cell level using mass cytometry. Nat. Comm 8, 14069.

17. Van Lehn RC, Atukorale PU, Carney RP, Yang Y, Stellacci F, Irvine DJ, & Alexander-Katz A (2013) Effect of Particle Diameter and Surface Composition on the Spontaneous Fusion of Monolayer-Protected Gold Nanoparticles with Lipid Bilayers. Nano Lett. 13, 4060–4067. [PubMed: 23915118]

18. Van Lehn RC, Ricci M, Silva PHJ, Andreozzi P, Reguera J, Voitchovsky K, Stellacci F, Alexander-Katz A (2014) Lipid tail protrusions mediate the insertion of nanoparticles into model cell membranes. Nat. Comm 5, 4482.

19. Acuna GP, Bucher M, Stein IH, Steinhauer C, Kuzyk A, Holzmeister P, Schreiber R, Moroz A, Stefani FD, Liedl T, et al. (2012) Distance Dependence of Single-Fluorophore Quenching by Gold Nanoparticles Studied on DNA Origami. ACS Nano 6, 3189–3195. [PubMed: 22439823]

20. Roux B (1995) The calculation of the potential of mean force using computer simulations. Comput. Phys. Commun 91, 275–282.

21. Kumar S, Rosenberg JM, Bouzida D, Swendsen RH & Kollman PA (1992) The weighted histogram analysis method for free-energy calculations on biomolecules. I. The method. J. Comput. Chem 13, 1011–1021.

22. Sunahara H, Urano Y, Kojima H & Nagano T (2007) Design and Synthesis of a Library of BODIPY-Based Environmental Polarity Sensors Utilizing Photoinduced Electron-Transfer-Controlled Fluorescence ON/OFF Switching. J. Am. Chem. Soc 129, 5597–5604. [PubMed: 17425310]

23. Bura T, Retailleau P, Ulrich G & Ziessel R (2011) Highly Substituted Bodipy Dyes with Spectroscopic Features Sensitive to the Environment. J. Org. Chem 76, 1109–1117. [PubMed: 21244077]

24. Arriaga LR, Lopez-Montero I, Monroy F, Orts-Fil G, Farago B, & Hellweg T (2009) Stiffening Effect of Cholesterol on Disordered Lipid Phases: A Combined Neutron Spin Echo + Dynamic Light Scattering Analysis of the Bending Elasticity of Large Unilamellar Vesicles. Biophys. J 96, 3629–3637. [PubMed: 19413968]

25. Sułkowski WW, Pentak D, Nowak K & Sułkowska A (2005) The influence of temperature, cholesterol content and pH on liposome stability. J. Mol. Struct 744–747, 737–747.

26. Leonenko ZV, Finot E, Ma H, Dahms TES & Cramb DT (2004) Investigation of Temperature-Induced Phase Transitions in DOPC and DPPC Phospholipid Bilayers Using Temperature-Controlled Scanning Force Microscopy. Biophys. J 86, 3783–3793. [PubMed: 15189874]

27. Jiang Y, Huo S, Mizuhara T, Das R, Lee Y-W, Hou S, Moyano DF, Duncan B, Liang X-J, & Rotello VM (2015) The Interplay of Size and Surface Functionality on the Cellular Uptake of Sub-10 nm Gold Nanoparticles. ACS Nano 9, 9986–9993. [PubMed: 26435075]

28. Boselli L, Polo E, Castagnola V & Dawson KA (2017) Regimes of Biomolecular Ultrasmall Nanoparticle Interactions. Angew. Chem. Int. Ed 56, 4215–4218.

29. Sousa AA, Hassan SA, Knittel LL, Balbo A, Aronova MA, Brown PH, Schuck P, & Leapman RD (2016) Biointeractions of ultrasmall glutathione-coated gold nanoparticles: effect of small size variations. Nanoscale 8, 6577–6588. [PubMed: 26934984]

30. Jackson AM, Myerson JW & Stellacci F (2004) Spontaneous assembly of subnanometre-ordered domains in the ligand shell of monolayer-protected nanoparticles. Nat. Mater 3, 330–336. [PubMed: 15098025]

31. Brust M, Walker M, Bethell D, Schiffrin DJ & Whyman R (1994) Synthesis of thiol-derivatised gold nanoparticles in a two-phase Liquid-Liquid system. J. Chem. Soc. Chem. Commun 0, 801–802.

32. Oostenbrink C, Villa A, Mark AE & Van Gunsteren WF (2004) A biomolecular force field based on the free enthalpy of hydration and solvation: The GROMOS force-field parameter sets 53A5 and 53A6. J. Comput. Chem 25, 1656–1676. [PubMed: 15264259]

33. Schmid N, Eichenberger AP, Choutko A, Riniker S, Winger M, Mark AE, & Van Gunsteren WF (2011) Definition and testing of the GROMOS force-field versions 54A7 and 54B7. Eur. Biophys. J 40, 843–856. [PubMed: 21533652]

34. Van Lehn RC & Alexander-Katz A (2013) Structure of Mixed-Monolayer-Protected Nanoparticles in Aqueous Salt Solution from Atomistic Molecular Dynamics Simulations. J. Phys. Chem. C 117, 20104–20115.

35. Song KC, Livanec PW, Klauda JB, Kuczera K, Dunn RC, & Im W (2011) Orientation of Fluorescent Lipid Analogue BODIPY-PC to Probe Lipid Membrane Properties: Insights from Molecular Dynamics Simulations. J. Phys. Chem. B 115, 6157–6165. [PubMed: 21513278]

36. Hess B, Kutzner C, van der Spoel D & Lindahl E (2008) GROMACS 4: Algorithms for Highly Efficient, Load-Balanced, and Scalable Molecular Simulation. J. Chem. Theory Comput 4, 435–447. [PubMed: 26620784]
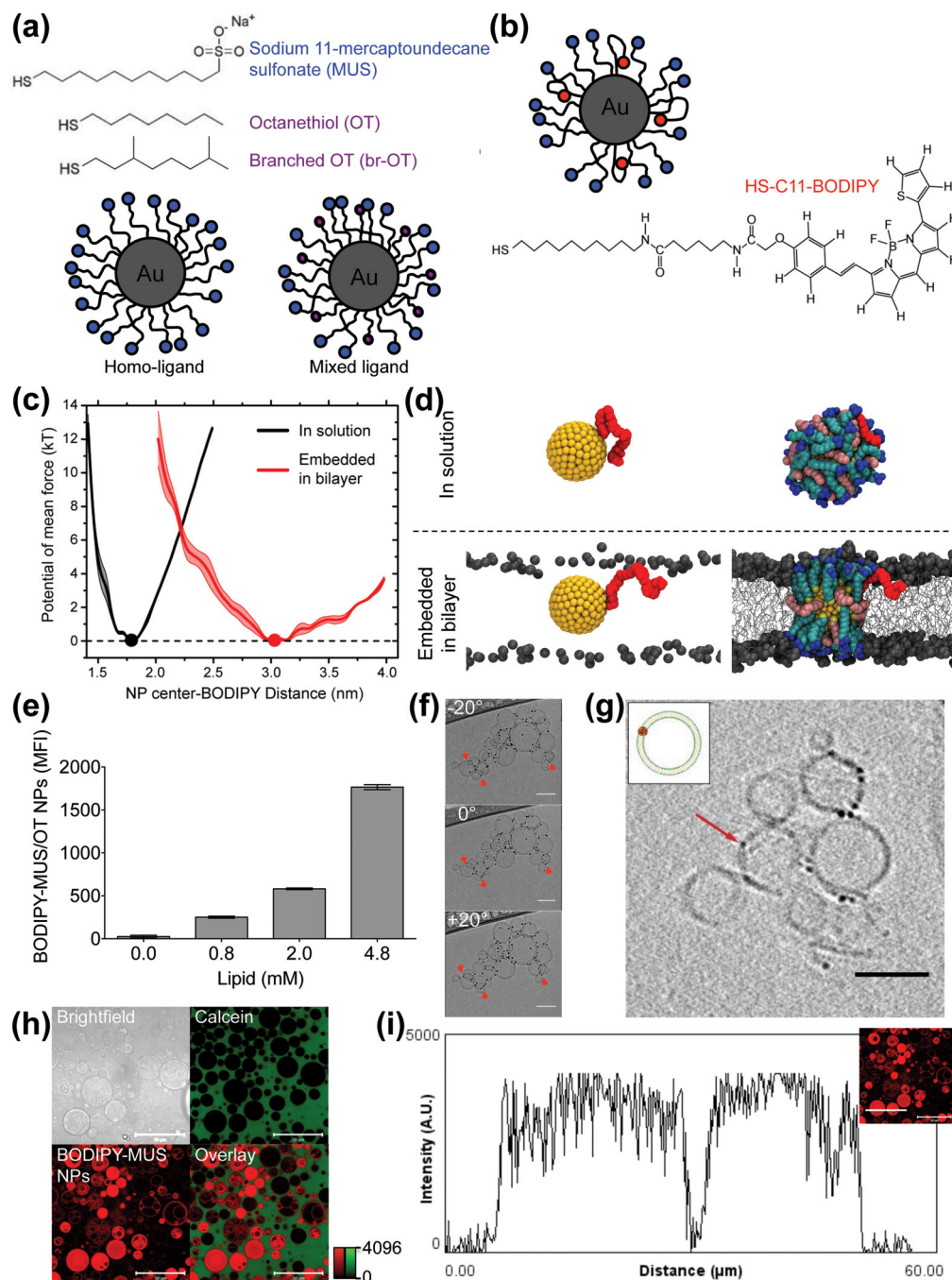
Figure 1. Nonpolar fluorophores tethered to amphiphilic NPs act as optical sensors for membrane embedding nanoparticles.
(**a**) Chemical structures of MUS, OT, and brOT organic ligands and schematic depiction of ligand-coated gold NPs. (**b**) Alkyl chain-tethered BODIPY dye structure and schematic depiction of BODIPY-labeled NPs in solution. (**c-d**) Molecular dynamics simulations of 2:1 MUS:OT NPs conjugated with 1 BODIPY ligand/particle, in aqueous solution or embedded in DOPC bilayers. Shown are (**c**) PMF measurements from atomistic molecular dynamics simulations (mean ± standard error from 2 independent runs) and (**d**) simulation snapshots

of BODIPY ligand configurations for particles in solution vs. bilayer-embedded. Left panel: cutaway view that depicts only the BODIPY ligand (red), Au core (yellow), and lipid headgroups (gray); Right panel: depicts all atoms involved (water molecules and ions are included in the simulations but not drawn for visual clarity). **(e)** MUS/OT NPs at 0.28 mg/mL (MUS:OT 2:1–2.5, Supplementary Table 1) were incubated for 1 hr at 25°C with DOPC liposomes at varying concentrations and BODIPY fluorescence was measured by fluorescence spectrometry (plotted as mean ± standard error, n=3). **(f)** Cryoelectron micrograph tilt series of MUS/OT NPs (0.28 mg/mL MUS/OT 1:1–2.6, Supplementary Table 1) incubated with DOPC liposomes overnight at 25°C (scale bars 50 nm, with red arrows indicating membrane-embedded NPs). **(g)** Single frame capture from a cryoelectron tomogram of DOPC liposomes incubated with 0.28 mg/mL MUS/OT NPs (MUS/OT 2:1–2.1, Supplementary Table 1) overnight at 25°C (scale bar 50 nm, with cartoon inset depiction of embedding and red arrow indicating an embedded NP). **(h)** Confocal micrographs of DOPC GMVs co-incubated with the membrane-impermeable dye calcein (20 μg/mL, green) and 0.28 mg/mL MUS NPs (MUS-2.4, Supplementary Table 1) labeled with BODIPY ligand (red) after 1 hr at 25°C (scale bar 50 μm). **(i)** Mean fluorescence intensity linescan of BODIPY signal from confocal micrograph in (**h**) (scale bar 50 μm).
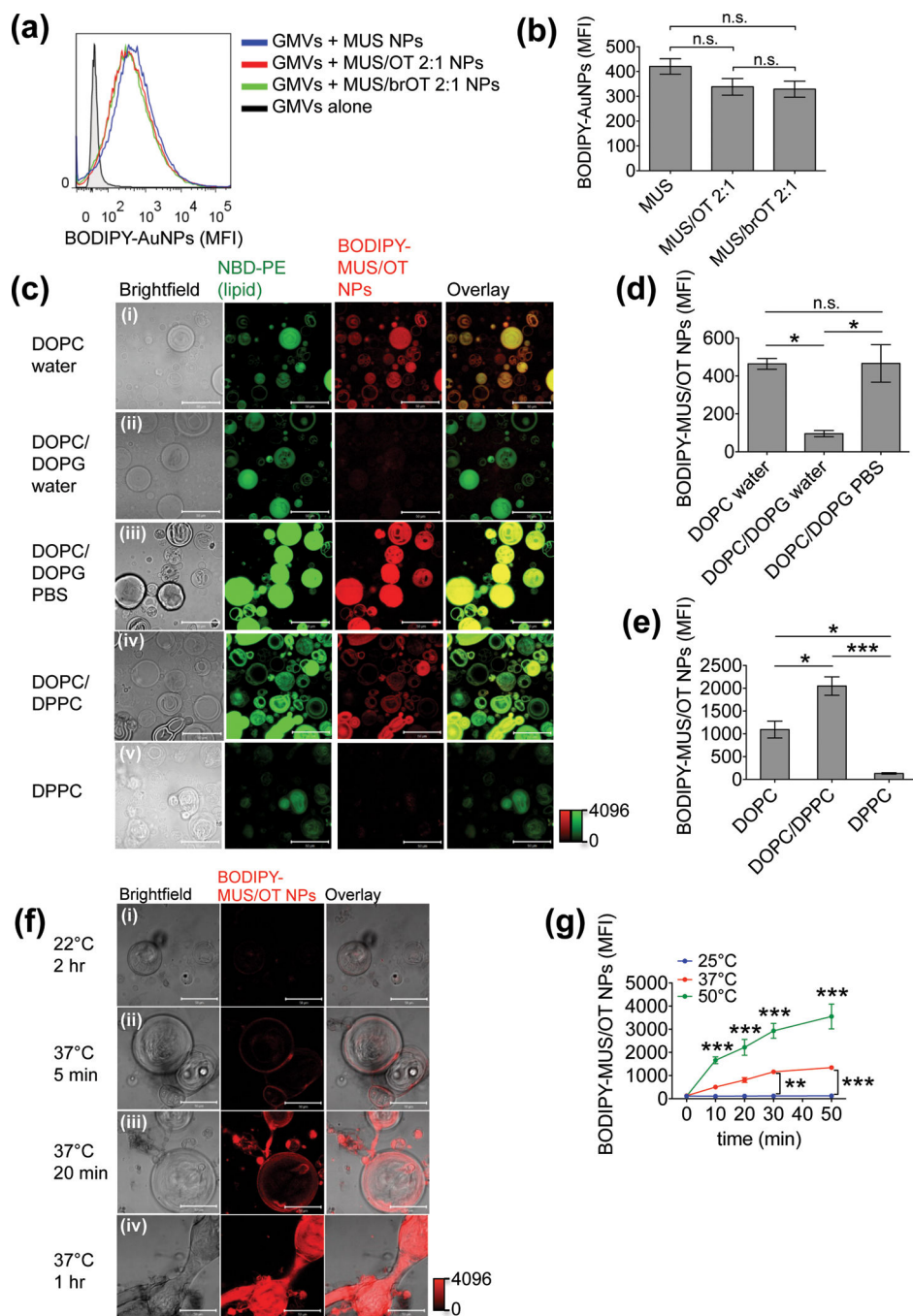
Figure 2. BODIPY fluorescence sensor reveals electrostatics and membrane fluidity govern NP penetration of lipid membranes.

(a, b) BODIPY-labeled NPs (0.28 mg/mL, MUS-1.7, MUS/OT 2:1–2.5, or MUS/brOT 2:1–2.4) were incubated with DOPC GMVs for 1 hr at 25°C, then analyzed by flow cytometry. Shown are **(a)** histograms of BODIPY fluorescence in GMVs and **(b)** mean fluorescence intensities from replicate samples, plotted as mean ± standard error (n=3) and not significant (n.s.) by one-way ANOVA with Bonferroni post-test. **(c)** Confocal micrographs of NBD-PE-labeled GMVs (green) incubated for 1 hr at 25°C with 0.28 mg/mL BODIPY-labeled NPs

(red, MUS:OT 1:1–2.6 for i-iii and MUS:OT 1:1–2.1 for iv-v). Shown are DOPC GMVs in water (i), 80:20 mol:mol DOPC:DOPG GMVs in water (ii), 80:20 mol:mol DOPC:DOPG GMVs in PBS (iii), 50:50 mol:mol DOPC:DPPC GMVs in water (iv), or DPPC GMVs in water (v). Scale bars 50 μm. **(d)** Quantification of confocal fluorescence signals from (c)(i-iii). Shown are mean ± standard error (n=3); *P < 0.05 by one-way ANOVA with Bonferroni post-test. **(e)** Quantification of flow cytometry analysis of (c)(iv-v). Shown are mean ± standard error (n=3); *P<0.05, ***P<0.001 by one-way ANOVA with Bonferroni post-test. **(f)** Confocal microscopy time course of DPPC GMVs incubated with BODIPY-labeled NPs (MUS:OT 2:1–2.5) at 25°C and 37°C (scale bars 50 μm). **(g)** Flow cytometry time course of BODIPY-labeled NPs (MUS:OT 2:1–2.5) incubated with DPPC GMVs at 25°C, 37°C, or 50°C. Shown is mean ± standard error (n=3) of BODIPY fluorescence associated with GMVs; ** P<0.01, *** P<0.001 by two-way ANOVA with Bonferroni post-test.
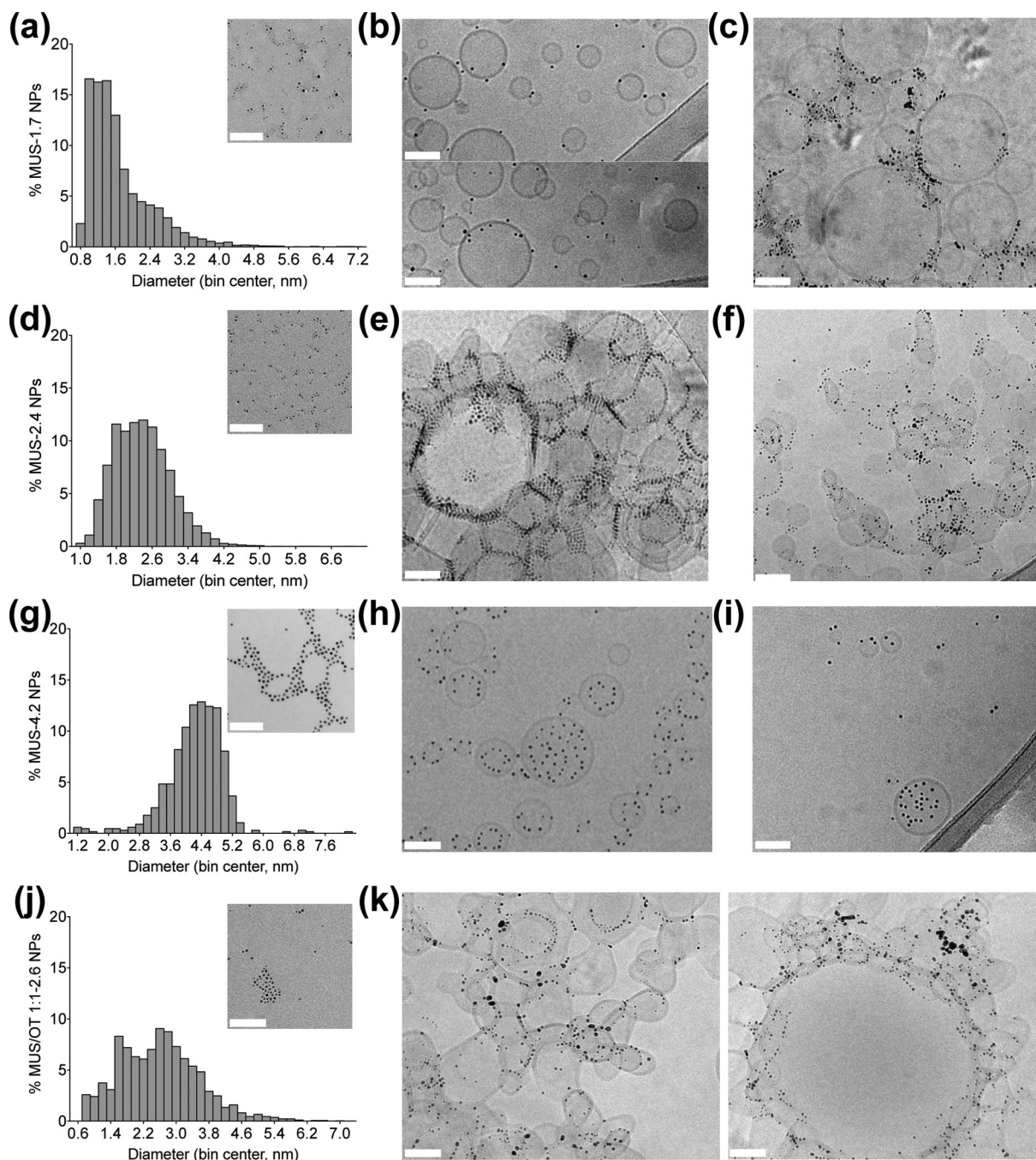
Figure 3. NP core size influences NP/liposome interactions at the nanoscale, including the mediation of membrane fusion.

Amph-NPs were incubated at 25°C with DOPC liposomes (1.5 mM lipid, 84±13 nm diameter) at 25°C then vitrified and imaged by cryoEM. **(a)** Core size distribution for MUS-1.7 particles, scale bar for TEM inset 50 nm. **(b, c)** CryoEM imaging of liposomes incubated for 1 hr with MUS-1.7 NPs (**b**, 0.28 mg/mL; **c**, 0.56 mg/mL). Scale bars 50 nm. **(d)** Core size distribution for MUS-2.4, scale bar for TEM inset 50 nm. **(e, f)** CryoEM imaging of liposomes incubated for 1 hr with MUS-2.4 NPs (**e**, 0.28 mg/mL NPs; **f**, 0.56

mg/mL NPs). Scale bars 50 nm. **(g)** Core size distribution for MUS-4.2, scale bar for TEM inset 50 nm. (**h, i**) CryoEM imaging of liposomes incubated 12 hr at 25°C with MUS-4.2 NPs (**h**, 0.28 mg/mL; **i**, 0.56 mg/mL). Scale bars 50 nm. **(j)** Core size distribution for MUS/OT 1:1–2.6 (Supplementary Table 1), scale bar for TEM inset 50 nm. **(k)** CryoEM imaging of MUS/OT 1:1–2.6 (0.28 mg/mL) incubated with liposomes for 1 hr at 25°C, scale bar 50 nm for both panels.
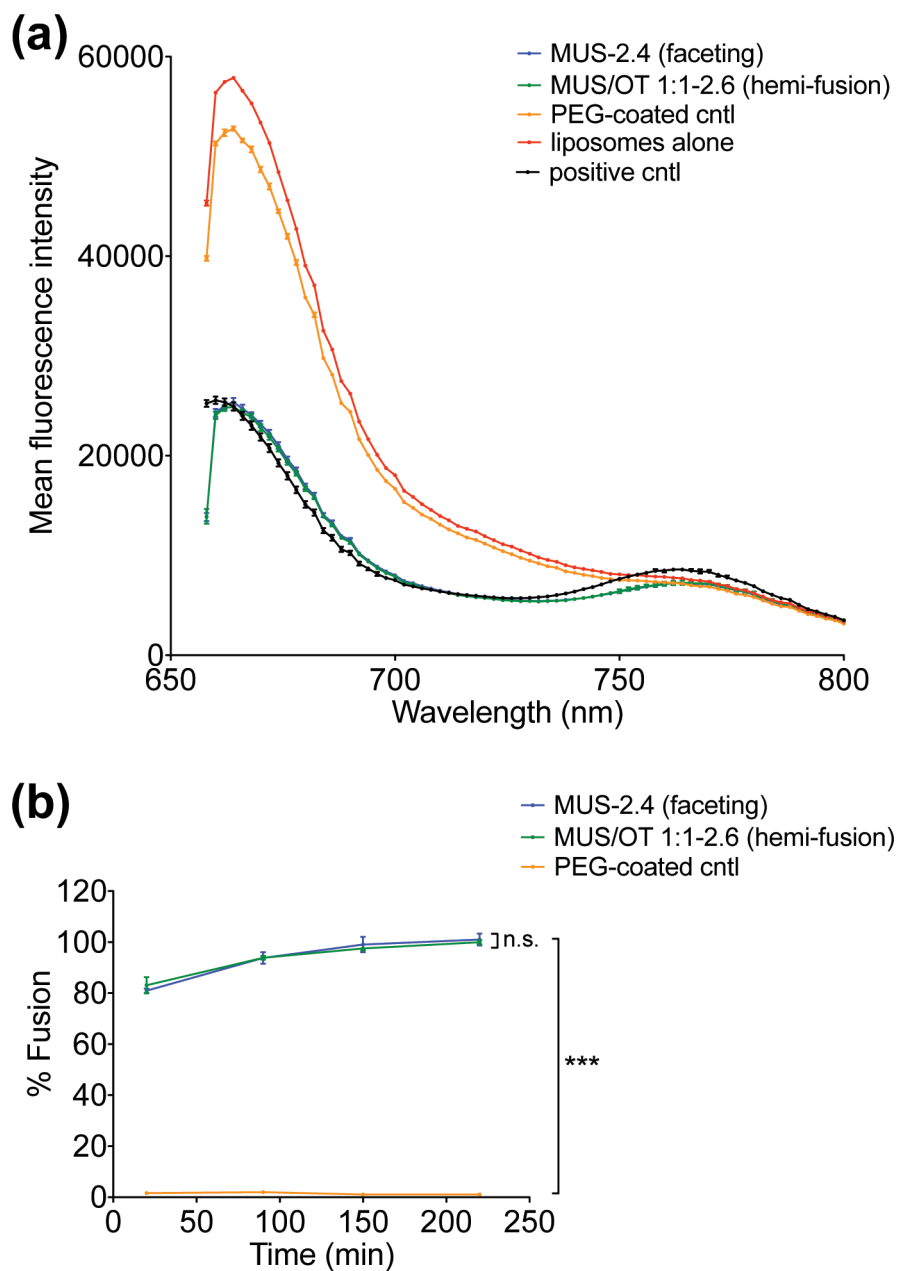
Figure 4. FRET analysis of liposome fusion mediated by NPs.
DOPC liposomes co-labeled with 0.1 mol% DiD and DiR (1.5 mM total lipid) were incubated with NPs (0.28 mg/mL MUS-2.4, MUS/OT 1:1–2.6, or PEG-coated control NPs) over a time course at 25°C, excited at 644 nm, and emission spectra were recorded from 658–800 nm. **(a)** Fluorescence emission intensity as a function of wavelength (mean ± standard error, n=3) at 20 min. **(b)** Percentage of liposome fusion determined from the ratio of acceptor to donor emission (Em764/Em660) for each sample over time. Data plotted as background-subtracted mean ± standard error (n=3) with statistics by two-way ANOVA with Bonferroni post-test (*** P<0.0001).